Chemical propulsion of hemozoin crystal motion in malaria parasites

Erica M. Hastings[a,1], Tomasz Skora[b,1], Keith R. Carney[c], Henry C. Fu[d], Tamara C. Bidone[a,b,e], and Paul A. Sigala[a,2]

[a]Department of Biochemistry, University of Utah School of Medicine, Salt Lake City, UT 84112
[b]Scientific Computing and Imaging Institute, University of Utah, Salt Lake City, UT 84112
[c]Huntsman Cancer Institute, University of Utah, Salt Lake City, UT 84112
[d]Department of Mechanical Engineering, University of Utah, Salt Lake City, UT 84112
[e]Department of Biomedical Engineering, University of Utah, Salt Lake City, UT 84112
[1]These authors contributed equally to this work

[2]Corresponding author: Paul Sigala
Phone number: (801) 587-4874
Email: p.sigala@biochem.utah.edu

Author Contributions: EMH and PAS designed and coordinated the study. EMH performed all experimental assays including parasite culture, microscopy, FV expansion, hemozoin isolation, and peroxide assays. EMH performed all SPT. EMH, KC, and TS scripted image analysis codes. EMH, TS, HF, and TCB scripted simulation codes. EMH and TS analyzed SPT data. EMH, TS, HF, TCB, and PAS interpreted data. EMH, TS, HF, TCB, and PAS wrote and/or edited the manuscript.

Competing Interest Statement: The authors declare no competing interests.

Preprint server: https://www.biorxiv.org/content/10.1101/2025.04.25.650681v1
(CC-BY-NC-ND license)

Classifications: Physical Sciences- Biophysics and Computational Biology,
Biological Sciences- Microbiology

Key words: Plasmodium, nanoparticle dynamics, Brownian diffusion, hydrogen peroxide catalysis, digestive vacuole

Abstract:

Malaria parasites infect red blood cells where they digest host hemoglobin and release free heme inside a lysosome-like organelle called the food vacuole. To detoxify excess heme, parasites form hemozoin crystals that rapidly tumble inside this compartment. Hemozoin formation is critical for parasite survival and central to antimalarial drug activity. Although the static structural properties of hemozoin have been extensively investigated, crystal motion and its underlying mechanism have remained puzzling. We used quantitative image analysis to determine the timescale of motion, which requires the intact vacuole but does not require the parasite itself. Using single particle tracking and Brownian dynamics simulations with experimentally derived interaction potentials, we found that hemozoin motion exhibits unexpectedly tight confinement but is much faster than thermal diffusion. Hydrogen peroxide, which is generated at high levels in the food vacuole, has been shown to stimulate the motion of synthetic metallic nanoparticles via surface-catalyzed peroxide decomposition that generates propulsive kinetic energy. We observed that peroxide stimulated the motion of isolated crystals in solution and that conditions that suppress peroxide formation slowed hemozoin motion inside parasites. These data suggest that surface-exposed metals on hemozoin catalyze peroxide decomposition to drive crystal motion. This work reveals hemozoin motion in malaria parasites as a biological example of an endogenous self-propelled nanoparticle. This mechanism of propulsion likely serves a physiological role to reduce oxidative stress to parasites from hydrogen peroxide produced by large-scale hemoglobin digestion during blood-stage infection.

Significance statement:

Hemozoin crystal formation is a major antimalarial drug target as it is essential for survival of *Plasmodium* parasites that cause malaria, one of the world's most devastating infectious diseases. Hemozoin crystals rapidly tumble inside the parasite food vacuole, and the mechanism and significance of this motion have been mysterious. Using quantitative live-cell imaging and computational modeling, we discovered that hemozoin motion is driven by catalytic decomposition of hydrogen peroxide on the crystal surface, a mechanism analogous to synthetic nanomotors. Hemozoin crystals have been viewed as inert detoxification products. Our work reframes the physiological role of these crystals as catalytically active nanoparticles whose mechanism of propulsion helps to neutralize toxic hydrogen peroxide generated by parasite digestion of hemoglobin during blood-stage infection.

85 **Main text:**

86 **Introduction:**

87 Malaria remains a deadly infectious disease that kills over 600,000 people each year and is
88 caused by *Plasmodium* parasites that invade and destroy red blood cells (RBCs) (1). During blood-
89 stage infection, parasites digest most of the RBC hemoglobin within an acidic food vacuole (FV)
90 that is similar to a mammalian lysosome (2). Hemoglobin proteolysis releases large quantities of
91 the iron-containing cofactor, heme, which parasites detoxify by forming multiple ~500 nm brick-
92 shaped hemozoin crystals within the ~1 μm-radius FV (**Fig. 1A**) (3, 4). The biocrystallization of
93 heme is a critical parasite survival strategy and major antimalarial drug target, such that free heme
94 that escapes incorporation into crystals is thought to underpin chloroquine activity and serve as the
95 key activator of frontline artemisinin therapies (5, 6).

96 Within the FV organelle, hemozoin crystals dynamically tumble in a rapid and unpredictable
97 fashion (***SI Appendix,*** **Movie S1**) (7-10). Although ubiquitous, these dynamics are sparsely studied
98 and have been described as Brownian in nature (7, 8). However, prior chemical and genetic
99 perturbations of the FV have provided evidence that hemozoin motion can be stopped, suggesting
100 additional energy inputs beyond thermal diffusion (***SI Appendix,*** **Movie S2, Fig. S1A**) (9-11).
101 Previous studies also provide conflicting evidence about whether hemozoin tumbling requires a
102 physiologically active cell and thus serves as a biomarker of parasite viability or responds to local
103 properties of the FV environment independent of the parasite (7-10). Therefore, uncovering the
104 physical nature and causative mechanism of crystal dynamics is key to unlocking a full
105 understanding of hemozoin and its critical function in malaria parasite survival and drug
106 susceptibility.

107

108 **Results:**

109 **Hemozoin tumbling occurs on ms timescale.** The rapid movement of hemozoin crystals is a
110 hallmark of RBC infection by *P. falciparum*, which is the most virulent parasite species in Africa
111 and causes nearly all human malaria deaths. To determine the timescale of hemozoin dynamics
112 within the FV, we imaged *P. falciparum*-infected RBCs with brightfield microscopy using
113 progressively faster frame rates (***SI Appendix,* Fig. S1B**). We observed that the pixel intensity
114 change between consecutive frames within the FV region decreased with increasing frame rate
115 until plateauing at ~200 frames per second (Δt = 5 ms) (**Fig. 1B**). This observation indicates that
116 the fastest detectable displacements of hemozoin crystals occur on a 5 ms timescale. Therefore,
117 we used a frame rate of ≥200 frames per second for all subsequent imaging.

118

119 **Hemozoin motion is a local FV property.** To better understand the nature and origin of hemozoin
120 motion within the FV, we sought to quantify the movement of individual crystals. Single-particle
121 tracking (SPT) was unsuccessful due to crystal congestion and spatially overlapping trajectories
122 in live parasites. To overcome this challenge, we developed an alternative method that quantified
123 the mean squared pixel intensity change (TAMSI) within the FV as a function of elapsed time,
124 which we define as "pixel velocity" (**Fig. 1C, *SI Appendix,* Movie S3, Fig. S2A-C**). This analysis
125 revealed >10-fold differences between hemozoin motion in live versus dead (drug-inactivated)
126 parasites, suggesting that the physiological condition of the FV underpins crystal dynamics (**Fig.
127 1D, *SI Appendix,* Fig. S2D**). To further probe the biological requirements for hemozoin motion,
128 we fractionated parasites and tested various conditions for crystal motion. We measured hemozoin
129 crystal TAMSI in fractionated intact parasites and isolated FVs and observed nearly identical pixel
130 velocities across all conditions except dead parasites (**Fig. 1D, *SI Appendix,* Fig. S2A-D**). These

131 findings indicate that hemozoin motion is a local property of the biochemically active FV
132 environment and independent of the parasite's cellular context. However, this motion stops in
133 lethally drug-treated parasites, suggesting a loss in FV membrane integrity and/or physiological
134 activity in dead parasites.
135
136 **Single-particle tracking of crystal motion.** To overcome FV congestion and enable accurate
137 single-particle tracking (SPT) analysis of crystal displacements, we expanded the vacuoles using
138 hypotonic conditions previously observed to enlarge mammalian lysosomes (12-14). This
139 expansion increased FV radii from ~1 μm to ~3 μm while preserving the rotational and
140 translational components of hemozoin crystal motion (**Fig. 2A, *SI Appendix,* Fig. S3A, Movie**
141 **S4**). Critically, the trajectories of individual crystals within expanded FVs could be reliably tracked
142 for up to half a second (≥ 100 frames) to enable detailed analyses of their motion (**Fig. 2A**).
143 Within expanded FVs, we collected over 3500 trajectories of individual hemozoin crystals
144 and analyzed their time-averaged mean squared displacements (TAMSDs) (***SI Appendix,* Fig.**
145 **S3C**). The weighted average of these TAMSDs as a function of elapsed time showed an anomalous
146 nonlinear time dependence with a diminishing slope (**Fig. 2B-C**). This observation contradicts
147 predictions for simple diffusion based on the Einstein-Smoluchowski equation, where the TAMSD
148 increases linearly with time (MSD = 4Dt) (15-18). Instead, the TAMSD data for hemozoin crystals
149 in the FV were best fit by a power law (MSD = $4\Gamma t^{\alpha}$), with an α value <1 indicative of subdiffusion
150 (**Fig. 2C**) (19).
151 To compare the anomalous motion of FV hemozoin crystals to conditions where purely
152 diffusive motion is expected, we isolated hemozoin crystals and suspended them in aqueous
153 solutions of variable viscosity (**Fig. 2A**). Viscosity within the parasite FV is unknown but expected

154 to be similar to a mammalian lysosome, ~100 – 400 cP (20-23). Based on these values, we
155 estimated the viscosity of expanded vacuoles due to water influx to be 10 – 40 cP, whose lower
156 limit is equal to the viscosity of 60% w/v glycerol (aq) (***SI Appendix,* Fig. S3B**). As expected, SPT
157 of isolated hemozoin crystals or inert nanobeads in water or 60% glycerol displayed a linear time
158 dependence ($\alpha \sim 1$), consistent with pure diffusion, while hemozoin motion within expanded FVs
159 exhibited nonlinear behavior ($\alpha = 0.64 \pm 0.12$) (**Fig. 2B, *SI Appendix,* Table S1, Fig. S3B**).

160 Based on fits to the power law form of the Einstein-Smoluchowski equation, hemozoin
161 within expanded FVs had a generalized diffusion coefficient (Γ) of ~ 0.17 $\mu m^2/s^\alpha$, which was
162 intermediate between that of isolated hemozoin in water (~ 1.1 $\mu m^2/s^\alpha$, 1 cP) and in 60% glycerol
163 (~ 0.10 $\mu m^2/s^\alpha$, 10 cP). The enhanced (faster) diffusion of hemozoin in FVs compared to 60%
164 glycerol was particularly prominent, given the expectation that both environments have similar
165 viscosities. Possible explanations for this difference in slope include inaccuracy in FV viscosity,
166 which may be less than 10 cP, or the presence of additional factors within the FV that stimulate
167 crystal motion.

168 To test the accuracy of our estimated viscosity in expanded FVs, we analyzed the
169 distribution of normalized crystal step sizes ($\mu m/s^{1/2}$) for hemozoin in expanded FVs, 60%
170 glycerol (10 cP), or a thinner solution of 40% glycerol (4 cP). For a spherical particle of radius 0.2
171 μm, Brownian motion theory predicts a characteristic distribution of particle steps centered around
172 ~ 0.6 $\mu m/s^{1/2}$ at a viscosity of 10 cP or ~1.2 $\mu m/s^{1/2}$ at 4 cP (15-18). We observed a most frequent
173 step size of ~ 0.6 $\mu m/s^{1/2}$ for hemozoin in expanded FVs and isolated crystals in 60% glycerol
174 (**Fig. 2D, *SI Appendix,* Fig. S3D-E**). In contrast, isolated crystals in 40% glycerol displayed a
175 recurring step size of ~1.2 $\mu m/s^{1/2}$ that was two-fold larger than FV hemozoin (***SI Appendix,* Fig.**
176 **S3D-E**). The close agreement between peak frequency of hemozoin step sizes within expanded

177 FVs and 60% glycerol (10 cP) and disagreement with the larger average step sizes in 40% glycerol
178 (4 cP) strongly support the conclusion that expanded FVs have an effective viscosity of 10 cP and
179 that the motion of FV hemozoin is faster than predicted for thermal diffusion at this viscosity.

180 Further dissection of the histograms revealed that hemozoin in expanded FVs exhibited a
181 heavier tail of longer step sizes compared to crystals in 60% glycerol (**Fig. 2D**). To quantify this
182 difference, we attempted to fit both distributions to a single population of moving particles. The
183 60% glycerol histogram was accurately fit by this model, which indicated a single population of
184 particles with a diffusion coefficient of ~ 0.17 $\mu m^2/s$. However, the same fit to the histogram of
185 crystals in expanded FVs could not be explained by a single population and instead revealed that
186 the distribution was more accurately decomposed into two populations, with 33% of crystals
187 having an expected diffusion coefficient (D_1) of 0.13 $\mu m^2/s$ and 67% of crystals with a much higher
188 (faster) diffusion coefficient (D_2) of 0.63 $\mu m^2/s$ (***SI Appendix,* Fig. S3E, Table S5**). Since D_1 is
189 close to the expected D for thermal diffusivity in 60% glycerol, we interpret the first population as
190 purely diffusive particles. The second, faster-moving population for FV hemozoin suggests either
191 that the size variation of hemozoin crystals differed between FVs and the glycerol environment or
192 that an additional energy source transiently accelerates crystal diffusion within the FV. To analyze
193 the potential for size heterogeneity, we solved for the expected particle size at the faster diffusion
194 coefficient. This analysis indicated that most particles would have to be smaller than the diffraction
195 limit of light (radius of ~ 0.03 μm) to account for faster diffusion and therefore unlikely to be seen
196 or tracked through a brightfield microscope (24). Based on these findings, we conclude that the
197 *Plasmodium* food vacuole viscosity is indeed similar to a mammalian lysosome and that crystal
198 motion deviates from our simplified experimental models of Brownian diffusion with additional
199 features of both confined and stimulated motion.

200

201 **Simulated multi-particle crystal motion.** Hemozoin crystals within the parasite FV have a
202 cuboidal shape, are confined by the surrounding FV membrane, and interact with each other due
203 to spatial crowding. These biophysical features differ from isolated crystals in solution or simple
204 spheres modeled by the Einstein-Smoluchowski equation for simple Brownian motion. To
205 determine if differences in crystal shape, FV boundary effects, and/or particle-particle interactions
206 contribute to the faster but constrained diffusion of FV hemozoin, we performed stochastic
207 Brownian dynamics simulations (25). These simulations incorporated interaction potentials and
208 boundary conditions designed to mimic expanded FV environments (***SI Appendix,* Fig. S4A**).
209 Specifically, we simulated diffusive motion of both hemozoin-shaped bricks and spherical
210 particles under dimensional confinement conditions similar to those in our experiments and
211 analyzed their trajectories to determine TAMSD values (***SI Appendix,* Movie S5-S6, Table S6**).
212 Cuboid bricks were modeled using surface-covering nodes with volume exclusion enforced by a
213 repulsive Lennard-Jones potential (**Fig. 3A-B**). Simulations of spherical particles included both
214 attractive and repulsive terms of the Lennard-Jones potential. This potential was parameterized
215 from experimental SPT data of FV hemozoin using the Direct Boltzmann Inversion method and
216 exhibited a very shallow minimum of -0.24 kcal/mol ($\ll k_B T$) at 0.82 μm, indicating weak
217 attraction between crystals (**Fig. 3B, *SI Appendix,* Fig. S4B-C**) (26).

218 Simulated TAMSDs were adjusted to account for the static localization error in the
219 experimental trajectories resulting from microscope noise that systematically offsets the observed
220 particle position from the true position (27). After making this correction, we observed a strong
221 concordance between the simulated models and experimental SPT analysis of isolated hemozoin
222 in water and 60% glycerol over 0.5 s (**Fig. 3C**). Using the power-law form of the Einstein-

223 Smoluchowski equation to fit the simulated data, we determined α exponents of ≥0.85 and ≥0.98
224 for crystal motion at viscosities equal to water and 60% glycerol, respectively, despite particle-
225 particle interactions and confinement within a spherical boundary of ~2.5 μm radius (***SI Appendix,***
226 **Tables S6 - S8**). These results closely matched the experimental data for isolated hemozoin in
227 these environments. Simulated TAMSDs in water showed a slight curvature toward subdiffusive
228 behavior, consistent with the expectation that particles reach the simulated boundary sooner in this
229 lower-viscosity environment. Most importantly, the α exponents in simulations were still
230 significantly greater than the α exponent obtained experimentally for FV hemozoin (0.64 ± 0.12)
231 (**Fig. 3C**, ***SI Appendix,*** **Fig. S4C, Tables S6 – S8**). These findings suggest that differences in
232 hemozoin shape, FV boundary constraints, and interactions between hemozoin crystals do not
233 explain the faster and nonlinear time dependence of FV hemozoin motion.
234
235 **Propulsion and micro-confinements explain hemozoin motion.** To understand the enhanced
236 diffusivity and constrained TAMSD properties of FV hemozoin compared to isolated crystals, we
237 further analyzed their TAMSD and normalized step-size distribution (**Fig. 2B,D**). The nonlinear
238 shape of the hemozoin TAMSD in FVs aligns with theoretical predictions for particle diffusion
239 where the TAMSD plateaus at ~ $0.8R^2$ within a sphere of radius R projected onto a 2D plane (**Fig.**
240 **4A**) (28). This prediction matches simulations of hemozoin in a FV-like environment but does not
241 account for hemozoin motion in expanded FVs where the TAMSD levels off at values that are
242 much smaller than expected (**Fig. 3C**). This discrepancy suggests that physical micro-
243 confinements within the FV limit crystal motion to sub-compartments of ~ 1.1 μm radius that are
244 2-fold smaller than the expanded FV radius (~ 2.5 μm) (***SI Appendix,*** **Tables S6, S8**). These

245 additional barriers may be due to membranous remnants of vesicles that deliver host hemoglobin
246 to the FV or other heterogeneities in the FV matrix that confine crystals (29).

247 The enhanced diffusivity and heavy tails of longer step sizes of FV hemozoin suggested
248 the possibility of energy inputs beyond thermal energy driving crystal motion (**Fig. 2D**). We first
249 ruled out that white light of variable brightness affected hemozoin motion, as changing microscope
250 light intensity from 1.8 to 25.3 mW/cm^2 did not alter the anomalous exponent or diffusion
251 coefficients in expanded vacuoles (***SI Appendix,*** **Fig. S5A**). We next tested a potential chemical
252 origin for the enhanced diffusivity of FV hemozoin. Hydrogen peroxide (H_2O_2) is produced within
253 the aerobic FV of parasites as a byproduct of hemoglobin digestion. This catabolic process releases
254 ferrous heme, which oxidizes to form hemozoin and generates hydrogen peroxide from ambient
255 O_2 (30, 31). Malaria parasites do not encode catalase to degrade FV hydrogen peroxide, and how
256 they neutralize this oxidative and cytotoxic stress remains unclear. Iron and other metals have been
257 shown to catalyze hydrogen peroxide decomposition to release kinetic energy (32-36). We
258 hypothesized that catalysis of this reaction within the FV by surface-exposed metals on hemozoin
259 stimulates crystal motion.

260 We tested this hypothesis by first asking if hemozoin catalyzed H_2O_2 decomposition. We
261 utilized an in vitro activity assay that used a surfactant to trap and visualize the O_2 gas bubbles
262 generated by this reaction (37). Both parasite-derived and synthetic hemozoin (β-hematin) but not
263 inert nanobeads produced visible foaming, but bubbling by parasite hemozoin was notably stronger
264 than synthetic crystals prepared from commercially sourced heme (***SI Appendix,*** **Fig. S6**). This
265 result supports the conclusion that both parasite and synthetic hemozoin catalyze H_2O_2
266 decomposition but that parasite hemozoin has higher activity.

267 We next tested whether 15% H_2O_2 enhanced the diffusivity of isolated parasite hemozoin
268 crystals in water. Using SPT, we observed a nearly 2-fold increase in the diffusion coefficient,
269 which is comparable to previously reported motion enhancements for metallic nanoparticles based
270 on this reaction (**Fig. 4B, *SI Appendix,* Fig. S5B, Table S1**) (38, 39). A milder enhancement was
271 observed for synthetic hemozoin crystals, but this "boost" was not observed for inert nanobeads in
272 water (**Fig. 4B, *SI Appendix,* Fig. S5B, Fig. S7, Tables S1, S3**). These motion enhancements
273 matched the relative reactivities of H_2O_2 with parasite hemozoin, synthetic hemozoin, or inert
274 nanobeads observed by the in vitro activity assay (***SI Appendix*, Fig. S6**). Power-law analysis of
275 parasite hemozoin motion showed that 15% H_2O_2 did not substantially alter the α exponent from
276 its value in water ($\alpha \sim 1$) indicating enhanced diffusion (**Fig. 2C, *SI Appendix,* Table S1**).
277 However, the step-size histogram for isolated hemozoin crystals in 15% H_2O_2 displayed a heavy
278 tail of longer step sizes, surprisingly similar to the histogram of FV hemozoin but in contrast to
279 isolated parasite hemozoin in 60% glycerol (**Fig. 2D, Fig. 4C**). The experimental step-size
280 histogram for isolated hemozoin in water (1 cP) was accurately fit to a single population with a
281 diffusion coefficient of 1.44 $\mu m^2/s$ at a particle radius of 0.15 μm. In 15% H_2O_2, the histogram of
282 crystal step sizes could only be accurately fit with a bimodal model where 38% of the crystal
283 population had $D_1 \sim 0.9$ $\mu m^2/s$ and the other 62% of crystal step sizes fit a $D_2 \sim 5.8$ $\mu m^2/s$ (***SI***
284 ***Appendix,* Fig. S5C**). The close similarity between D_1 and the thermal diffusion coefficient
285 expected for 0.2 μm radius particles (1.1 $\mu m^2/s$) suggests a smaller population of purely diffusive
286 crystals and a larger population of crystals whose ≥5-fold larger D_2 value resembles the
287 enhancement ratio observed for FV hemozoin (***SI Appendix,* Table S5, Fig. S5C**).
288 We next investigated whether the crystal population with enhanced diffusivity could be
289 explained by a simple model of random propulsion due to hemozoin surface catalysis of H_2O_2

290 decomposition. As a minimal model, we simulated 0.2 μm radius spherical particles undergoing
291 thermal diffusion (D ~ 1.1 $\mu m^2/s$ in water) and subject to randomized propulsive velocities
292 normally distributed around zero. For translational propulsive velocity, we found that choosing a
293 standard deviation of 60 μm/s for each direction (x, y, z) produced a step-size distribution that
294 matched the faster fraction in the bimodal fit. Combining the step-size distribution of this active
295 population (62%) with that of a thermally diffusing population (D_1 ~ 0.9 $\mu m^2/s$, 38%) produced a
296 step-size distribution like that observed experimentally (**Fig. 4C, *SI Appendix,* Fig. S5D**). Thus,
297 our model for active propulsion of hemozoin by random catalysis of peroxide decomposition is
298 sufficient to explain the experimental bimodal step-size distribution.

299 We next tested whether simulated particles in the estimated FV viscosity, with a smaller
300 radial boundary of 1.1 μm and a bimodal distribution of step sizes parametrized from our hemozoin
301 results in 15% H_2O_2, could quantitatively account for the enhanced diffusion and anomalous
302 constraints of FV hemozoin. Inclusion of either the 1.1 μm radial boundary or the bimodal step-
303 size distribution in simulations failed to match experiments, but including both properties nearly
304 quantitatively matched the experimental TAMSD (**Fig. 4D**). The strong agreement between
305 simulations and experiments supports our hypothesis that sub-compartmental constraints and
306 chemical stimulation quantitatively explain the enhanced and anomalous features of FV crystal
307 motion.

308 Our model predicts that a reduction in H_2O_2 concentration will suppress crystal motion.
309 Since hydrogen peroxide generation in the parasite FV is expected to depend on delivery of
310 oxyhemoglobin to this compartment by ingestion of RBC hemoglobin (31)(40), we reasoned that
311 lowering ambient oxygen tension would diminish oxyhemoglobin levels and reduce H_2O_2
312 concentration in the FV. To test the effect of this reduction on crystal motion, we determined pixel

313 velocities (TAMSI) for hemozoin moving within parasites grown and maintained at ambient 20%
314 O_2 or at reduced O_2 tension of 2% expected to lower oxyhemoglobin levels by 80% (***SI Appendix,***
315 **Fig. S5E**). Critically, parasites have a low respiratory requirement for O_2 and grow similarly in
316 these two conditions (41). In contrast to unchanged parasite growth, there was a ~2-fold reduction
317 in pixel velocity for hemozoin motion in live parasites in 2% O_2 that remained faster than observed
318 for dead parasites (**Fig. 4E**). This decrease in speed directly supports our model that H_2O_2 serves
319 as a fuel for propelling crystal motion in the FV and that lowering peroxide concentration slows
320 hemozoin dynamics.
321
322 **Discussion:**
323 Hemozoin formation is both an essential survival mechanism and critical axis of drug
324 activity against blood-stage malaria parasites. Although major structural properties of hemozoin
325 are well studied, the rapid tumbling of these crystals within the parasite FV has remained a major
326 enigma and defied experimental dissection. Our study incisively unravels the origin of this motion,
327 which is both faster than diffusion and subject to surprisingly tight physical confinement (**Fig. 4F**).
328 Quantitative analysis of hemozoin movement provides a unique probe that has revealed
329 structural obstacles within the FV matrix that constrain crystal displacements to regions that are
330 smaller than FV boundaries. We hypothesize that these constraints may reflect membrane
331 remnants of hemoglobin-uptake vesicles or other physical heterogeneities within the FV milieu
332 similar to recent biophysical observations in yeast cytoplasm (29, 42). While the static nature of
333 the *P. falciparum* FV has been visualized extensively by electron microscopy, the dynamic
334 biophysical properties of this environment have remained inaccessible. Our analysis of hemozoin
335 motion provides a rigorous estimate of 100-200 cP for the effective viscosity of the FV matrix that

336 is similar to a mammalian lysosome. We anticipate that the experimental and computational
337 approaches developed in this study will enable future studies of the FV to further test and refine
338 understanding of this critical compartment and its key biochemical functions relevant for parasite
339 physiology and antimalarial drug activity.

340 Hemozoin has been viewed canonically as a chemically inert detoxification product within
341 the parasite FV (43, 44). Our results reframe the physiological role of these crystals and support
342 the biological paradigm that metal-catalyzed H_2O_2 decomposition on the surfaces of hemozoin
343 generates a random propulsive force to boost crystals towards larger steps that enhance diffusion
344 while maintaining an unpredictable trajectory. This propulsive chemical mechanism is well-
345 documented for synthetic metallic nanomachines, but *Plasmodium* hemozoin provides an
346 unprecedented biochemical example of endogenous nanoparticle self-propulsion in cells (38, 39).
347 Additional biological phenomena with this mechanism are likely to exist.

348 *Plasmodium* parasites do not encode a catalase enzyme, and mechanisms to neutralize the
349 oxidative and cytotoxic stress of H_2O_2 production in the FV due to hemoglobin catabolism have
350 been uncertain. Prior studies suggest possible roles for RBC-derived human catalase as well as
351 parasite glutathione in reducing vacuolar H_2O_2 stress (30, 45). We propose that catalytic
352 decomposition of peroxide on the surface of hemozoin also contributes substantially to H_2O_2
353 detoxification within the FV. Chemical strategies that interfere with hydrogen peroxide
354 decomposition on the surface of hemozoin are therefore predicted to reduce crystal motion and
355 increase oxidative stress for parasites that sensitizes them to therapeutic strategies targeting this
356 vacuole. This hypothesis is consistent with prior works which reported that knockdown of a
357 lipocalin-like protein in the FV diminished hemozoin tumbling and impaired parasite growth via
358 oxidative stress that was reversed by the antioxidant Trolox (9, 10). The mechanistic connection

359 between this lipocalin-like protein and hemozoin motion remains undefined but may involve
360 differential exposure of surface metals on hemozoin due to altered crystal morphology and/or
361 surface interactions in the absence of lipocalin.

362 The surface chemistry of catalytic H_2O_2 decomposition by metallic nanoparticles is
363 complex (46), but our results provide initial insights into surface features of hemozoin that
364 underpin this reaction in the FV. Hemozoin contains pentacoordinate iron within heme molecules
365 that may be accessible at crystal surfaces and contribute to weak catalytic breakdown of H_2O_2 (3,
366 47-49). Differences in average crystal dimensions and surface area between synthetic and parasite-
367 derived hemozoin may contribute to their apparent reactivity differences with H_2O_2. Parasite-
368 derived hemozoin also has additional surface complexity and contains adhered lipids, proteins,
369 and metals whose abundance and detection can vary with purification method and stringency (50).
370 The higher apparent reactivity of H_2O_2 with parasite hemozoin than synthetic hemozoin may
371 suggest that additional metals on the surface of parasite-derived crystals contribute to its stronger
372 activity (***SI Appendix,* Fig. S6- S7**). Prior elemental analyses have detected calcium, silicon, and
373 iron on the surface of parasite hemozoin (48, 51). Our previous work also suggests the presence
374 of labile iron within the FV (52). Labile iron adhered to hemozoin crystals may underpin its
375 enhanced activity with H_2O_2 compared to synthetic hemozoin. Surface-bound calcium or silicon,
376 which do not catalyze H_2O_2 decomposition but enhance catalysis by other transition metals, may
377 also contribute (53). The ability of metal chelators like EDTA and deferoxamine to quench
378 catalytic H_2O_2 decomposition by parasite hemozoin supports a key role for surface labile metals
379 (***SI Appendix*, Fig. S6**). We have ongoing interests and experiments to further understand
380 hemozoin surface chemistry. It also remains an important future challenge to deeply understand
381 the oxidative chemistry in the parasite FV that underpins H_2O_2 generation in this compartment.

382 Finally, dynamic motion of hemozoin within the FV matrix disperses crystals and
383 maximizes their surface area available for biomineralization of labile heme released from
384 hemoglobin proteolysis. Indeed, simple calculations suggest that crystal aggregation may reduce
385 the exposed surface area up to 70%, and photodynamic ablation of hemozoin motion causes
386 crystals to aggregate (***SI Appendix*, Fig. S8, Movies S7-S10**), as previously described (11).
387 Multiple studies have also reported that isolated hemozoin crystals have an intrinsic tendency to
388 clump after purification (54-56). These observations are consistent with the interaction potentials
389 between crystals determined in this study from single particle tracking that indicated a shallow
390 minimum at 0.82 μm, suggesting a weak attraction at the contact distance between crystals (**Fig.
391 3B**). Thus, hemozoin motion may serve an additional physiological role to maximize the exposed
392 surface area of hemozoin crystals and to enhance the rate of heme detoxification within the FV,
393 especially during peak stages of hemoglobin digestion.
394

395 **Materials and methods:**

396 ***SI Appendix,* Figures S1-S9, Tables S1-S8, Movies S1-S10**

397

398 **Cell culture**

399 *Parasite culturing*

400 *P. falciparum* Dd2 (42) and NF54 (57) parasites were grown in human red blood cells received
401 from the University of Utah Hospital blood bank at 90% N_2, 5% CO_2, and 5% O_2 at 37°C in RPMI
402 1640 containing AlbuMAXI (Thermo Fisher Scientific) supplemented with glutamine (2%
403 hematocrit), as previously described (58). Medium was changed daily. Parasitemia was measured
404 by Giemsa-stained blood smear or by flow cytometry (58). Parasites were routinely synchronized
405 to the early ring stage by treatment with 5% D-sorbitol. All imaging of hemozoin motion was
406 performed using late trophozoite- and schizont-stage parasites (36-48 hours post synchronization).

407

408 *Parasite fractionation*

409 Intact parasites within a permeabilized RBC ghost and isolated food vacuoles were prepared by
410 membrane lysis. Parasitized red blood cells were permeabilized with 0.05% saponin in PBS, as
411 described previously (58). This treatment released the hemoglobin contents in the RBC but
412 maintained the membrane of isolated intact parasites. The plasma membrane of isolated parasites
413 was permeabilized with exposure to ice-cold acidic hypotonic buffer (20 mM MES, pH 4.5),
414 transferred to a watch glass on ice, mixed forcefully through a 27-G needle, and centrifuged at
415 15,800xg. The supernatant was removed by vacuum aspiration, and the pellet was resuspended in
416 intracellular solution (120 mM KCl, 10 mM NaCl, 25 mM HEPES, 2 mM $MgCl_2$, 5 mM Na_2HPO_4,

417 pH 7.3) and triturated with a 27-G needle, as previously described (59). Isolated food vacuoles
418 were resuspended on ice and imaged within 20 mins of isolation.
419
420 *Inhibitor treatments*
421 Parasites were magnet purified (isolating schizont stages) and incubated for 6 hours with fresh red
422 blood cells. Newly invaded red blood cells were treated with 5% D-sorbitol (isolating ring stages)
423 to produce rings with a 6-hour synchrony window. Parasites were separated into different wells
424 and treated with high concentrations of inhibitors to induce cell death. Parasites were treated
425 continuously with 0.2 μM WR99210 (Jacobus Pharmaceuticals) after ring synchronization (IC_{50}:
426 0.043 μM); 0.1 μM chloroquine (Sigma-Aldrich) at 30 hours post-synchronization (IC_{50}: 0.024
427 μM); 0.2 μM artemisinin (Sigma-Aldrich) at 30 hours post synchronization (IC_{50}: 0.032 μM); or
428 200 μM 5-aminolevulinic acid (ALA, Sigma-Aldrich) at 24 hours post synchronization followed
429 by 1 min of light exposure after 12 hours of ALA incubation (11, 60). Parasites were imaged at 36
430 hours post-synchronization and were scored based on moving vs. static hemozoin crystals. Thirty
431 parasites were counted for each replicate and three replicates were taken for each drug treatment.
432 Image analysis and TAMSI quantification was performed on chloroquine-treated parasites,
433 although similar results were obtained for all drug-treatment conditions.
434
435 *Synthetic hemozoin*
436 Beta-hematin (synthetic hemozoin, sHz) was synthesized by adding 47.5 mg hemin (Sigma-
437 Aldrich, H9039-1G) into 10 mL of 0.1N NaOH. Heme was precipitated slowly by adding 3.5 mL
438 of glacial acetic acid dropwise. Tubes were incubated for 6 hours at 80ºC and washed with 100
439 mM sodium bicarbonate, pH 9.1, as previously described (61).

440

441 *Foaming Assay*

442 Hydrogen peroxide decomposition leads to formation of water (H_2O) and molecular oxygen (O_2).
443 In a microcentrifuge tube, 1% Triton X-100, water, and 15% H_2O_2 (final concentration) were
444 added to 10 µL of packed pellet. Sample pellets included polystyrene nanobeads (NB), parasite
445 hemozoin (pHz), synthetic hemozoin (sHz), parasite hemozoin with metal chelators (100 µM of
446 deferoxamine (DFO, Sigma-Aldrich) or ethylenediaminetetraacetic acid (EDTA, Sigma-Aldrich))
447 and 100 units catalase (Sigma, C9332-1G). As a qualitative approach, trapped oxygen gas from
448 this reaction was visualized as foam after 40 mins incubation, as previously described (37).
449 Hydrogen peroxide concentration was confirmed by UV-vis absorbance spectroscopy (62).

450

451 **Microscopy**

452 *Widefield microscopy*

453 Live parasites were imaged with a Nikon Ti-E inverted widefield microscope equipped with an
454 Andor Zyla CMOS camera and 100X PlanAPO oil immersion objective. All pixel analysis time
455 lapses were taken at ≥300 fps, while all single-particle tracking time lapses were taken ≥200 fps
456 (slower frame rate due to larger region of interest). Microscope slides were incubated for 5 mins
457 of "rest" after sample mounting and before imaging to minimize drift/bulk fluid flows under the
458 microscope. All time lapse images were compiled as .nd2 files. Samples containing infected RBCs
459 at 12-15% trophozoite or schizont parasitemia were mounted on a standard 75 x 25-mm glass
460 microscope slide. For imaging, 7 µL of the resuspended culture was deposited on a slide and
461 covered with a 22 x 40-mm coverslip. Even pressure was applied to the sample to remove excess
462 liquid and the coverslip was sealed with clear nail polish to prevent evaporation. Low oxygen

463 condition samples were imaged with flat-bottom dishes (CellTreat, #229632) on the same
464 microscope, to ensure a sealed incubator that maintained low oxygen concentrations
465
466 *Low O_2 environment*
467 An OKOLAB stage incubator on the Nikon Ti-E microscope was used with a dish adaptor. The
468 clear lid was sealed with parafilm and flushed with CO_2 for 20 minutes before images were
469 collected. Samples were measured by an FD-103 Waterproof and Shockproof O_2 Meter (Forensics
470 Detectors) with a tube connection to the sealed incubator. Meter had range between 0-30% O_2 with
471 resolution within 0.1% O_2 within $<$ 1 minute.
472
473 *Expanded vacuoles*
474 Infected red blood cells were incubated in 100 µl of media diluted 1:1 with deionized water at
475 37°C for 20 mins before imaging. For imaging, 7 µL was deposited on a slide and sealed with a
476 coverslip. Expanded vacuoles that retained hemozoin motion were imaged as described above.
477
478 *Hemozoin isolation*
479 A culture of infected RBCs at 1-20% parasitemia was saponin treated and resuspended in cold
480 PBS. Parasites were spun down at 15,000xg for 5 mins, and resuspended in 2% SDS. Crystals
481 were centrifuged at 15,000xg for 5 mins and resuspended in room temperature PBS with 2 µl of
482 Qiagen protease and incubated for 1 hour at 37°C. Crystals were then washed with 2% SDS and
483 spun at 15,000xg for 5 mins. Crystals were finally resuspended in 6M urea and stored in 4°C until
484 imaging. Crystal pellets were washed twice and resuspended by vortexing in 100% water or 40-
485 60% glycerol/water (w/v) concentrations for imaging.

486

487 *H_2O_2 addition*

488 30% H_2O_2 (Fisher, BP2633-500) was removed from a freshly opened bottle and mixed 1:1 with
489 an equal volume of hemozoin crystals or nanobeads resuspended in water to give a final
490 concentration of 15% H_2O_2 and immediately mounted onto a microscope slide. The viscosity of
491 30% H_2O_2 is 1.25 cP, which after mixing with water results in a final effective viscosity of 1.12
492 cP (63).

493

494 *Light intensity*

495 Light intensity on the Nikon Ti-E inverted widefield microscope was measured by a power meter
496 sensor placed in the sample focal plane with a ThorLabs PM100A power meter analog console.
497 Intensity was adjusted by with Sola automated LED lightsource.

498

499 *Glycerol ratios and viscosity calculations*

500 100% glycerol was added by weight converted to volume to distilled water to make aqueous
501 glycerol solutions at room temperature (w/v). Solutions were vortexed for ≥ 1 hour to ensure
502 adequate mixing. Viscosities were calculated from the simple Stokes-Einstein equation:

503 $$D = \frac{k_B T}{6\pi\eta r}$$

504 Where D is the diffusion coefficient derived from temperature (T), Boltzmann constant (k_B),
505 viscosity of surrounding medium (η) and the hydrodynamic radius of the particle (r). Viscosity
506 values were solved by single-particle tracking control nanobeads with defined radius 0.4 μm at
507 room temperature (22°C) and then computing and fitting the time-averaged mean squared
508 displacement (TAMSD):

509 $$\mathrm{TAMSD}(t) = 4Dt + \sigma$$

510 Where t is elapsed time. This model accounts for static localization error inherent to SPT data by
511 introducing constant factor σ (27). Experimentally determined viscosities for nanobeads in the
512 respective glycerol concentrations were nearly identical to literature values for these conditions
513 (64). The effective viscosity from hypotonic expansion of vacuoles was estimated by using a
514 weighted average:

515 $$\text{Average viscosity of expanded vacuole} = \frac{x_1 w_1 + x_2 w_2}{w_1 + w_2}$$

516 Where x is the estimated or calculated viscosity and w is percent of total expanded volume with
517 that expected viscosity. We estimated wild type food vacuoles had viscosities similar to lysosomes
518 (100 – 400 cP) and that the increase in volume from swelling was due solely to the influx of water
519 (1 cP). We estimated that 90% of the swollen volume was water with 10% of the final volume
520 having the original 100 cP lysosome viscosity, creating an effective 10 cP viscosity for the
521 expanded vacuole.

522

523 *Photodynamic ablation of hemozoin motion in parasites*

524 Infected red blood cells were photosensitized by adding 200 µM exogenous 5-aminolevulinic acid
525 (ALA) and incubated for 18 hours. This treatment results in an accumulation of the phototoxic
526 intermediate protoporphyrin IX (PPIX), as previously published (11). Live parasites were imaged
527 with a Nikon Ti-E inverted widefield microscope as described above, before and after light
528 activation. Parasites were subjected to light activation by 1 min exposure to ~450 nm light.

529

530 **Image analysis**

531 *Time-averaged mean squared pixel change intensity (TAMSI)*

532 Single-particle tracking (SPT) proved challenging due to crystal congestion and overlapping
533 trajectories within the small volume of the FV, limiting tracking to only a few frames. To overcome
534 these limitations, we developed an alternative metric to assess crystal mobility: the time-averaged
535 mean squared pixel intensity change (TAMSI) within the FV area as a function of elapsed time.
536 Beyond approximately 0.2 s, TAMSI reached a plateau, indicating that crystal movement had fully
537 decorrelated and longer elapsed times no longer contributed to increased pixel intensity changes.
538 We empirically fit this time-dependent change to a power law growth function to determine the
539 average characteristic time at which 50% of the plateau value was reached (see *Fitting* Methods
540 and ***SI Appendix,* Fig. S9**):

541 $$< [\Delta I(t)]^2 >= C(1 - \frac{1}{(t/\tau_0)^\alpha + 1})$$

542 This analysis allowed us to define an apparent pixel velocity by dividing the TAMSI by the average
543 characteristic time of ~0.18 s, which we observed in native, living parasites. To compare between
544 different FV-imaging conditions, we used the ~0.18 s characteristic time to determine the pixel
545 velocity for all time lapse experiments. Datasets were saved as .nd2 files and processed through
546 MATLAB version R2021a with the Bio-Formats toolbox (65). Each frame of a dataset was
547 adjusted so that bottom and top 1% pixel intensities were saturated to create better image contrast.
548 The dataset was flipped to return the complement pixel intensities of each frame and the region of
549 interest was defined manually by tracing the outer membrane of the food vacuole discernable in
550 brightfield images. Each pixel intensity change was calculated by:

551 $$\mathrm{TAMSI(t)} = < [\Delta I(t)]^2 > = < [I(\tau + t) - I(\tau)]^2 >_\tau$$

552 Where $I(t)$ stands for pixel intensity, and the angle brackets denote averaging over various τ
553 values and over all pixels. Each squared change was averaged over every pixel in the region of
554 interest for every elapsed time τ and plotted as a function of increasing elapsed time.

555

556 *Fitting*

557 We observed nonexponential relaxation of pixel intensity change as a function of elapsed time.

558 We used a general power law in the following form:

559 $$< [\Delta I(t)]^2 >= C(1 - \frac{1}{(t/\tau_0)^\alpha + 1})$$

560 to empirically fit to the experimental data. The relaxation time τ_0 encodes the time t at which pixel

561 intensity change reaches half of its asymptotic value C to which the function tends in the limit of

562 $t \rightarrow \infty$. We used `scipy.optimize.curve_fit` function in Python to empirically fit our data

563 (66). For dead parasites, the dominant contribution to pixel intensity fluctuation was the

564 background noise that deviated from the power law equation used for conditions with moving

565 hemozoin. Since we observed noise as the dominant feature, we instead used only the first term of

566 expansion of the power law in Poiseux series (for $\alpha = 0.5$, $C = 0.05$):

567 $$< [\Delta I(t)]^2 >= 0.05\sqrt{t/\tau_0}$$

568 Before fitting, we subtracted from the experimental data the short-time average computed between

569 5th and 15th data points. Then, we performed fitting from the 10th data point onwards, where we

570 observed an extremely slow increase. As the number of particles in a small pixel is governed by

571 Poisson distribution, it depends only on the total intensity divided by the number of pixels. For

572 long times t the Poisson random variables are going to be statistically independent, and in principle

573 C can be predicted from the Skellam distribution properties (67). Thus, we expected C to be

574 comparable between dead and living parasites. Thus, the choice of α and C were based on the

575 median values observed for the infected red blood cell group.

576

577 **Single-particle tracking**

578 *TrackMate*

579 We used the Fiji plugin TrackMate to single-particle track hemozoin crystals throughout time lapse
580 images (68, 69). We chose the LoG (Laplacian of a Gaussian) detector as our method of
581 localization. This method applies a LoG filter to each image to find local maxima with quadratic
582 fitting for sub-pixel localization. We estimated our object diameter to be 0.6 μm unless tracking
583 the defined 0.8 μm diameter nanobeads. Each time lapse was manually processed by resetting the
584 initial thresholding to rule out background spots. We used the Simple LAP tracker because we
585 assumed there would be no branching tracks (particles were not breaking and reforming). We used
586 0.5 μm as our linking max distance, 0.5 μm for our gap-closing max distance, and 2 as our gap-
587 closing max frame gap. Tracks were minimally filtered by particle spots that were "stuck" where
588 their displacements did not increase with time.

589

590 *Time-averaged mean squared displacement*

591 For each system, we recorded numerous tracks of different length (number of time points), and
592 different time resolution (differing from experiment to experiment). To analyze such
593 heterogeneous dataset, we first computed and stored all displacements, i.e., $r(i+j) - r(j);\ i, j \in$
594 $\mathbb{N}$, and used them as a basis for the subsequent analyses. To compute time-averaged mean squared
595 displacements (TAMSD), we iterated over the list of displacements, squared them, and averaged
596 ones belonging to equal lag i. To i=1, we attributed a timestep averaged over all experiments
597 belonging to the same system. To compute uncertainties, we repeated the computation of squared
598 displacements (SD) but limiting the computation only to those displacements which are
599 statistically independent. For instance, for the same particle, r(3)-r(0) is not statistically
600 independent from r(5)-r(2). Therefore, we used only these SDs for which start time j is a multiple

of the lag time i. For each lag time i, we stored a list of N_i statistically independent SDs. Subsequently, for each lag time i, we performed 100 random selections of N_i SD values from the list and used standard deviation of the means of the selected samples as a measure of uncertainty in TAMSD value. If there was only 1 value in the SD list, we attributed infinite uncertainty.

We fit TAMSD with two diffusion models:

Normal:

$$\text{TAMSD}\ (t) = 4Dt + \sigma$$

And anomalous:

$$\text{TAMSD}\ (t) = 4\Gamma t^{\alpha} + \sigma$$

We used the `scipy.optimize.curve_fit` function in `python` to empirically fit the data and provided the uncertainties as inverses of fitting weights. This means that in least squares optimization, the residuals are divided by the uncertainties, making the points with poor statistics weigh less. We fit only the short-time parts of the TAMSD curves (0.1-0.4 s). To ensure that using averaged timesteps did not distort the results, for the systems in which normal diffusion is expected, we divided all the squared displacements by the timestep:

$$\text{TAM}[\text{SD}/\Delta t]\ (\text{i}) = 4Di + \text{s}$$

This procedure led to very similar values (*SI Appendix,* Tables S2 and S4 compared to Tables S1 and S3, respectively).

Simulations

Control simulations for TAMSI comparison

We used $1/\tau_0$ as a proxy for the diffusion coefficient. To test the accuracy of this approximated value, we performed a series of point-particle Brownian dynamics simulations in which we computed pixel intensity change using the same protocol as when analyzing experimental data, but instead of computing intensity change we computed the number of particles in each pixel. We observed faster relaxation (smaller τ_0) for particles with higher diffusion coefficients D. Specifically, we performed Brownian dynamics simulations of 600 noninteracting particles of diffusion coefficients D = 2, 10, 20 $\mu m^2/s$ in a 20 nm × 20 nm × 20 nm box (with periodic boundary conditions) for 10000 steps (dt = 500 ps). Then, we divided the system into 100 2D pixels along X and Y dimensions and quantified the number of particles N in each pixel in time. We calculated:

$$< [\Delta N(t)]^2 >=< [N(\tau + t) - N(\tau)]^2 >_\tau$$

and averaged over the pixels. In agreement with Skellam distribution properties, the plateau occurred at twice the average number of particles in a single pixel, which is 2 × 600 / 100 = 12; τ_0 is the value of time at which pixel particle number fluctuation reaches a value of 6. We observed that τ_0 decreases with increase in diffusion coefficient, making its inverse a valid proxy for diffusivity. See Fig. S2d and Fig. S9 for results. A similar method was used recently employing a "countoscope" analysis (70). We noted that the simulations are scale invariant, so rescaling the length unit (in pixel size and diffusion coefficients) leads to the same results.

Brownian dynamics simulations

We performed Brownian dynamics simulations of hemozoin-like cuboidal "bricks" using a 1:1:3.5 ratio rectangular prism with dimensions 170x170x585 nm using custom MATLAB version R2021a code (54). Nodes were spaced ~80 nm apart to total 74 nodes on the surface of each brick. These nodes had regularized stokeslets applied and summed over the entire brick. We

646 calculated randomized rotational and translational steps based on the Stokes-Einstein equation for
647 spherical particles in low Reynolds number. Timestep was 0.0033 s to match timesteps of
648 experimental time lapses, temperature: 293.15 K. Confinement was realized by defining spherical
649 region of various radii and defining repulsive Lennard-Jones interaction between wall and
650 particles. Particle-particle interactions were defined by the same repulsive Lennard-Jones equation
651 with epsilon estimated from published literature ($\varepsilon = 0.08$ kcal/mol, $\sigma = 57$ nm):(71)

652 $$V_{LJ}(r;\ \varepsilon, \sigma) = 4\varepsilon[(\sigma/r)^{12}]$$

653 See Table S6 for physical parameters of each simulation, which mimicked experimental expanded
654 FV conditions.

655 Using a custom MATLAB version R2021a code,(54) we modeled a sphere with radius 0.2
656 µm undergoing thermal translational and rotational diffusion in water due to Langevin forces. In
657 addition, each sphere had propulsion due to chemical activity modeled by a fixed-body
658 translational and rotational velocity. The propulsive velocities of the population of spheres obeyed
659 normal distributions with mean zero. For rotational propulsive velocity, the normal distribution
660 had a standard deviation of 314 rad/s for all three directional components (x, y, z), which is
661 consistent with tumbling rotation speeds we observe in **Movie S4** (~ 168 – 419 rad/s). For
662 translational propulsive velocity, a standard deviation of 60 µm/s adequately reproduced the step-
663 size distribution for the active portion of the experimental bimodal distribution for hemozoin in
664 15% H_2O_2. We simulated 1000 trajectories up to 0.33 s to mimic experimental conditions.

665 We performed Brownian dynamics simulations of 40 spheres in confinement using
666 LAMMPS software (`fix brownian`) (72). Timestep was 1 µs, total number of steps was
667 20000000, and temperature: 293.15 K. Friction coefficients corresponding to 0%, 40%, and 60%
668 glycerol were: 1917.0, 7131.0, and 20704.0 g $mol^{-1}fs^{-1}$. These friction coefficients translate to a

669 hemozoin dynamic radius of 0.169 μm. Confinement was realized by defining spherical region of
670 radius 2.9 μm and defining a short-range harmonic repulsive interaction between wall and particles
671 ($\epsilon = 0.1$kcal/mol/Å^2, $\sigma = 0.1$μm). Simulations with "peroxide boost" were performed via custom
672 `python` code, using the distribution in step sizes from experimental data and implementing hard
673 spherical boundaries.
674
675 *Parametrizing experimental crystal-crystal interaction*
676 From tracks of hemozoin in the food vacuole, we computed histograms of distances between the
677 separate crystals P(r). We used the Direct Boltzmann Inversion (DBI) method (73) to parametrize
678 the potentials:

679 $$V(r) = -k_B T \, ln \, [P(r)/P_{ni}(r)]$$

680 where $P_{ni}(r)$ is the histogram as if the crystals would not interact at all (ideal gas). We modeled the
681 geometry underlying experimental data as a 3D sphere projected onto a 2D plane. Thus, to compute
682 $P_{ni}(r)$ we performed the following computation:
683
684 1. Random-uniform insertion of 10000 point particles into 3D sphere of radius 2.9 μm
685 2. Projection of coordinates onto the XY plane.
686 3. Computing distances between all particle projections.
687 4. Computing histogram of distances, with 100 bins spanning a range from 0.0 to 6.0 μm.
688
689 We fit a 6-12 Lennard Jones potential:

690 $$V_{LJ}(r;\ \varepsilon, \sigma) = 4\varepsilon[(\sigma/r)^{12} - (\sigma/r)^{6}]$$

to the resultant DBI potential for distances larger than 0.64 μm (to avoid large errors stemming from fitting to a very steep increase due to excluded volume). Parameters giving best match were: ε = 0.24±0.06 kcal/mol, σ = 0.643±0.008 μm.

To show the robustness of our results to a specific form of the potential, we also performed simulations with two different interaction potentials. First, we used Weeks-Chandler-Andersen (WCA) potential — LJ-based exclusively repulsive potential representing volume exclusion:

$$V_{LJ}(r;\ \varepsilon,\sigma) = 4\varepsilon[(\sigma/r)^{12} - (\sigma/r)^{6}] + \varepsilon \text{ for } r < 2^{1/6}\sigma \text{ and 0 otherwise.}$$

with ε and σ remaining the same as in DBI LJ potential. Second, we used Yukawa potential — exclusively repulsive potential with long-range repulsion:

$$V_{LJ}(r;\ \varepsilon,\sigma) = Ae^{\kappa r}/r$$

with A = 0.3 kcal/mol·μm, κ = 1 μm^{-1}. Global cutoff was set to 2 μm.

Jump distribution

To extend the analysis, we computed histograms of the displacement lengths divided by i$\Delta\tilde{r} = \Delta r/\sqrt{i\Delta t}$. For a Brownian motion, such histograms are governed by the following probability density function:

$$P(\Delta\tilde{r};\ D) = (2D)^{-1}\Delta\tilde{r}\ exp\ [-(\Delta\tilde{r})^2/4D]d\Delta\tilde{r}$$

This function has a maximum for $\Delta\tilde{r} = \sqrt{2D}$. For low-viscosity systems, we computed histograms for i=1 to maximize the sample size. For high-viscosity systems, we computed histograms for i=10 to avoid contributions of static localization error to the jump statistics. Static localization errors are inherent to SPT data, especially in high viscosity systems with confinement, where the accuracy between the observable particle position is slightly different than the particle's true position (27). We observed that fitting with the theoretical expression gives poor results, especially

at high-jump length heavy tails. To quantify these tails, we performed fitting with bimodal model, i.e.:

$$P_2(\Delta\tilde{r};\ D_1, D_2, c) = c(2D_1)^{-1}\Delta\tilde{r}\ exp\ [-(\Delta\tilde{r})^2/4D_1]d\Delta\tilde{r} + (1-c)(2D_2)^{-1}\Delta\tilde{r}\ exp\ [-(\Delta\tilde{r})^2/4D_2]d\Delta\tilde{r}$$

obtaining much better agreement with the experimental curves.

Data availability

All data described in the manuscript are shown in the figures and provided in SI Appendix. Supplementary movies are provided in figshare. All time lapses for data from pixel analysis (TAMSI) in Fig. 1B-D and Fig. 4E are provided in figshare:

Movies - RBCs. figshare. Dataset. https://doi.org/10.6084/m9.figshare.28719737.v1

Movies - RBCs low O2. figshare. Dataset. https://doi.org/10.6084/m9.figshare.28719716.v1

Movies - Isolated parasites. figshare. Dataset. https://doi.org/10.6084/m9.figshare.28719722.v1

Movies - Isolated FVs. figshare. Dataset. https://doi.org/10.6084/m9.figshare.28719734.v1

Movies - Dead parasites. figshare. Dataset. https://doi.org/10.6084/m9.figshare.28719731.v1

Movies - Expanded vacuoles. figshare. Dataset. https://doi.org/10.6084/m9.figshare.28719719.v1

Supplementary Movies. figshare. Dataset. https://doi.org/10.6084/m9.figshare.28835870.v2

Code availability

All MATLAB, `python`, and LAMMPS scripts used for data analysis and simulations, along with default parameters and all experimental single-particle tracks for step-size distribution and TAMSD analysis are available at https://github.com/emhastin/HemozoinMotion.git.

Acknowledgements:

We thank Kiarash Samsami, Ludivine Sanchez-Arias, and Sigala lab members for helpful discussions. We thank Xiang Wang, Mike Bridge, and Anton Classen at the Utah Cell Imaging Core Facility; Shawn Colby at the Health Sciences Machine Shop; and Brian Van Devener at the Utah Nanofab for experimental assistance. This work was supported by NIH grants R35GM133764 (PAS), R21AI185746 (PAS), and R35GM14749 (TCB); a pilot award from the Utah Center for Iron and Heme Disorders U54DK110858 (PAS); and a pilot award jointly funded by the Price College of Engineering and the 3i Initiative at the University of Utah (PAS, HF, and TCB). EMH was funded in part by NIH training grant T32AI055434. Brightfield microscopy and flow cytometry were performed using core facilities at the University of Utah.

Uncategorized References

1. P. Venkatesan, The 2023 WHO World malaria report. *Lancet Microbe* **5**, e214-e214 (2024).
2. J. M. Matz, Plasmodium's bottomless pit: properties and functions of the malaria parasite's digestive vacuole. *Trends Parasitol* **38**, 525-543 (2022).
3. S. Pagola, P. W. Stephens, D. S. Bohle, A. D. Kosar, S. K. Madsen, The structure of malaria pigment beta-haematin. *Nature* **404**, 307-310 (2000).
4. G. S. Noland, N. Briones, D. J. Sullivan, Jr., The shape and size of hemozoin crystals distinguishes diverse Plasmodium species. *Mol Biochem Parasitol* **130**, 91-99 (2003).
5. D. J. Sullivan, Jr., I. Y. Gluzman, D. G. Russell, D. E. Goldberg, On the molecular mechanism of chloroquine's antimalarial action. *Proc Natl Acad Sci U S A* **93**, 11865-11870 (1996).
6. L. Tilley, J. Straimer, N. F. Gnadig, S. A. Ralph, D. A. Fidock, Artemisinin Action and Resistance in Plasmodium falciparum. *Trends Parasitol* **32**, 682-696 (2016).
7. J. Wongtanachai, K. Silamut, N. P. Day, A. Dondorp, U. Chaisri, Effects of antimalarial drugs on movement of Plasmodium falciparum. *Southeast Asian J Trop Med Public Health* **43**, 1-9 (2012).
8. N. Sachanonta *et al.*, Ultrastructural and real-time microscopic changes in P. falciparum-infected red blood cells following treatment with antimalarial drugs. *Ultrastruct Pathol* **35**, 214-225 (2011).
9. J. M. Matz *et al.*, A lipocalin mediates unidirectional heme biomineralization in malaria parasites. *Proc. Natl. Acad. Sci. U. S. A.* **117**, 16546-16556 (2020).
10. P. C. Burda *et al.*, Structure-Based Identification and Functional Characterization of a Lipocalin in the Malaria Parasite Plasmodium falciparum. *Cell Rep* **31**, 107817 (2020).

11. P. A. Sigala, J. R. Crowley, J. P. Henderson, D. E. Goldberg, Deconvoluting heme biosynthesis to target blood-stage malaria parasites. *Elife* **4** (2015).
12. S. J. Hao, J. F. Hou, N. Jiang, G. J. Zhang, Loss of membrane cholesterol affects lysosomal osmotic stability. *Gen Physiol Biophys* **27**, 278-283 (2008).
13. L. Yang, G. J. Zhang, Y. G. Zhong, Y. Z. Zheng, Influence of membrane fluidity modifiers on lysosomal osmotic sensitivity. *Cell Biol Int* **24**, 699-704 (2000).
14. M. Hu, N. Zhou, W. Cai, H. Xu, Lysosomal solute and water transport. *J Cell Biol* **221** (2022).
15. F. R. S. H. M. R. S. E. R. I. A. V. P. L. S. R. Brown, XXVII. A brief account of microscopical observations made in the months of June, July and August 1827, on the particles contained in the pollen of plants; and on the general existence of active molecules in organic and inorganic bodies. *Philosophical Magazine Series 2* **4:21** (1828).
16. A. Einstein, Über die von der molekularkinetischen Theorie der Wärme geforderte Bewegung von in ruhenden Flüssigkeiten suspendierten Teilchen. *Annalen der Physik* **322**, 549-560 (1905).
17. W. Sutherland, A dynamical theory of diffusion for non-electrolytes and the molecular mass of albumin. *The London, Edinburgh, and Dublin Philosophical Magazine and Journal of Science* **9:54**, 781-785 (1905).
18. M. v. Smoluchowski, Zur kinetischen Theorie der Brownschen Molekularbewegung und der Suspensionen. *Annalen der Physik* **326**, 756-780 (1906).
19. L. F. Richardson, Atmospheric diffusion shown on a distance-neighbour graph. *P R Soc Lond a-Conta* **110**, 709-737 (1926).
20. T. Liu *et al.*, Quantitatively mapping cellular viscosity with detailed organelle information via a designed PET fluorescent probe. *Sci Rep* **4**, 5418 (2014).
21. M. K. Kuimova, Mapping viscosity in cells using molecular rotors. *Phys Chem Chem Phys* **14**, 12671-12686 (2012).
22. J. Devany, K. Chakraborty, Y. Krishnan, Subcellular Nanorheology Reveals Lysosomal Viscosity as a Reporter for Lysosomal Storage Diseases. *Nano Lett* **18**, 1351-1359 (2018).
23. D. Su, C. L. Teoh, N. Gao, Q. H. Xu, Y. T. Chang, A Simple BODIPY-Based Viscosity Probe for Imaging of Cellular Viscosity in Live Cells. *Sensors (Basel)* **16** (2016).
24. E. Abbe, Archiv für Mikroskopische Anat Entwicklungsmech. **9**, 413-468 (1873).
25. G. A. Huber, J. A. McCammon, Brownian Dynamics Simulations of Biological Molecules. *Trends Chem* **1**, 727-738 (2019).
26. W. G. Noid, Perspective: Coarse-grained models for biomolecular systems. *J Chem Phys* **139**, 090901 (2013).
27. S. C. Weber, M. A. Thompson, W. E. Moerner, A. J. Spakowitz, J. A. Theriot, Analytical Tools To Distinguish the Effects of Localization Error, Confinement, and Medium Elasticity on the Velocity Autocorrelation Function. *Biophysical Journal* **102**, 2443-2450 (2012).
28. M. Weiss, M. Elsner, F. Kartberg, T. Nilsson, Anomalous subdiffusion is a measure for cytoplasmic crowding in living cells. *Biophys J* **87**, 3518-3524 (2004).
29. A. Alder *et al.*, The role of Plasmodium V-ATPase in vacuolar physiology and antimalarial drug uptake. *Proc. Natl. Acad. Sci. U. S. A.* **120**, e2306420120 (2023).
30. S. E. Francis, D. J. Sullivan, Jr., D. E. Goldberg, Hemoglobin metabolism in the malaria parasite *Plasmodium falciparum*. *Annu. Rev. Microbiol.* **51**, 97-123 (1997).

31. H. Atamna, H. Ginsburg, Origin of reactive oxygen species in erythrocytes infected with Plasmodium falciparum. *Mol Biochem Parasitol* **61**, 231-241 (1993).
32. X. Ma *et al.*, Reversed Janus Micro/Nanomotors with Internal Chemical Engine. *ACS Nano* **10**, 8751-8759 (2016).
33. Y. Wang *et al.*, Bipolar electrochemical mechanism for the propulsion of catalytic nanomotors in hydrogen peroxide solutions. *Langmuir* **22**, 10451-10456 (2006).
34. D. L. Hitt, C. M. Zakrzwski, M. A. Thomas, MEMS-based satellite micropropulsion via catalyzed hydrogen peroxide decomposition. *Smart Mater Struct* **10**, 1163-1175 (2001).
35. S. Eloul, W. C. K. Poon, O. Farago, D. Frenkel, Reactive Momentum Transfer Contributes to the Self-Propulsion of Janus Particles. *Physical Review Letters* **124** (2020).
36. C. Bechinger *et al.*, Active Particles in Complex and Crowded Environments. *Rev Mod Phys* **88** (2016).
37. T. Iwase *et al.*, A simple assay for measuring catalase activity: a visual approach. *Sci Rep* **3**, 3081 (2013).
38. J. R. Howse *et al.*, Self-motile colloidal particles: From directed propulsion to random walk. *Physical Review Letters* **99** (2007).
39. R. Golestanian, T. B. Liverpool, A. Ajdari, Propulsion of a molecular machine by asymmetric distribution of reaction products. *Phys Rev Lett* **94**, 220801 (2005).
40. K. Becker *et al.*, Oxidative stress in malaria parasite-infected erythrocytes: host-parasite interactions. *Int J Parasitol* **34**, 163-189 (2004).
41. L. K. Basco, Cultivation of Asexual Intraerythrocytic Stages of Plasmodium falciparum. *Pathogens* **12** (2023).
42. R. M. Garner, A. T. Molines, J. A. Theriot, F. Chang, Vast heterogeneity in cytoplasmic diffusion rates revealed by nanorheology and Doppelganger simulations. *Biophys J* **122**, 767-783 (2023).
43. P. A. Sigala, D. E. Goldberg, The peculiarities and paradoxes of *Plasmodium* heme metabolism. *Annu. Rev. Microbiol.* **68**, 259-278 (2014).
44. L. M. Coronado, C. T. Nadovich, C. Spadafora, Malarial hemozoin: from target to tool. *Biochim Biophys Acta* **1840**, 2032-2041 (2014).
45. A. Willems, T. Oertel, P. D. Roepe, Redox Homeostasis within the Drug-Resistant Malarial Parasite Digestive Vacuole. *Biochemistry* **64**, 2247-2261 (2025).
46. R. Serra-Maia *et al.*, Mechanism and Kinetics of Hydrogen Peroxide Decomposition on Platinum Nanocatalysts. *ACS Appl Mater Interfaces* **10**, 21224-21234 (2018).
47. M. L. Kremer, The reaction of hemin with H2O2. *Eur J Biochem* **185**, 651-658 (1989).
48. E. D. Guerra *et al.*, Inorganic ions on hemozoin surface provide a glimpse into Plasmodium biology. *J Inorg Biochem* **200**, 110808 (2019).
49. P. B. Klar *et al.*, Cryo-tomography and 3D Electron Diffraction Reveal the Polar Habit and Chiral Structure of the Malaria Pigment Crystal Hemozoin. *ACS Cent Sci* **10**, 1504-1514 (2024).
50. T. Dalapati, J. M. Moore, Hemozoin: a Complex Molecule with Complex Activities. *Curr Clin Microbiol Rep* **8**, 87-102 (2021).
51. E. D. Guerra, F. Baakdah, E. Georges, D. S. Bohle, M. Cerruti, What is pure hemozoin? A close look at the surface of the malaria pigment. *J Inorg Biochem* **194**, 214-222 (2019).
52. K. M. Loveridge, P. A. Sigala, Identification of a divalent metal transporter required for cellular iron metabolism in malaria parasites. *Proc. Natl. Acad. Sci. U. S. A.* **121**, e2411631121 (2024).

53. A. L. Pham, C. Lee, F. M. Doyle, D. L. Sedlak, A silica-supported iron oxide catalyst capable of activating hydrogen peroxide at neutral pH values. *Environ Sci Technol* **43**, 8930-8935 (2009).
54. S. Kapishnikov *et al.*, Aligned hemozoin crystals in curved clusters in malarial red blood cells revealed by nanoprobe X-ray Fe fluorescence and diffraction. *Proc Natl Acad Sci U S A* **109**, 11184-11187 (2012).
55. M. Olivier, K. Van Den Ham, M. T. Shio, F. A. Kassa, S. Fougeray, Malarial pigment hemozoin and the innate inflammatory response. *Front Immunol* **5**, 25 (2014).
56. R. Sutanto, S. Mosalaganti, Uncovering the Absolute Structure of the Malarial Pigment Crystal, Hemozoin, Using Cryo-electron Tomography and Three-Dimensional Electron Diffraction. *ACS Cent Sci* **10**, 1439-1441 (2024).
57. T. Ponnudurai, A. D. Leeuwenberg, J. H. Meuwissen, Chloroquine sensitivity of isolates of Plasmodium falciparum adapted to in vitro culture. *Trop Geogr Med* **33**, 50-54 (1981).
58. S. Falekun *et al.*, Divergent acyl carrier protein decouples mitochondrial Fe-S cluster biogenesis from fatty acid synthesis in malaria parasites. *Elife* **10** (2021).
59. K. J. Saliba *et al.*, Acidification of the malaria parasite's digestive vacuole by a H+-ATPase and a H+-pyrophosphatase. *J. Biol. Chem.* **278**, 5605-5612 (2003).
60. L. M. Sanz *et al.*, P. falciparum in vitro killing rates allow to discriminate between different antimalarial mode-of-action. *PLoS One* **7**, e30949 (2012).
61. V. Thomas *et al.*, A novel way to grow hemozoin-like crystals in vitro and its use to screen for hemozoin inhibiting antimalarial compounds. *PLoS One* **7**, e41006 (2012).
62. L. J. McClelland, T. C. Mou, M. E. Jeakins-Cooley, S. R. Sprang, B. E. Bowler, Structure of a mitochondrial cytochrome c conformer competent for peroxidase activity. *Proc. Natl. Acad. Sci. U. S. A.* **111**, 6648-6653 (2014).
63. M. K. Phibbs, P. A. Giguere, Hydrogen peroxide and its analogues. I. Density, refractive index, viscosity, and surface tension of deuterium peroxide-deuterium oxide solutions. *Can J Chem* **29**, 173-181 (1951).
64. J. B. Segur, H. E. Oberstar, Viscosity of Glycerol and Its Aqueous Solutions. *Ind Eng Chem* **43**, 2117-2120 (1951).
65. J. W. Tay (2025) Bioformats Image Toolbox.
66. P. Virtanen *et al.*, SciPy 1.0: fundamental algorithms for scientific computing in Python. *Nat Methods* **17**, 261-272 (2020).
67. J. G. Skellam, The Frequency Distribution of the Difference between 2 Poisson Variates Belonging to Different Populations. *J Roy Stat Soc a Sta* **109**, 296-296 (1946).
68. D. Ershov *et al.*, TrackMate 7: integrating state-of-the-art segmentation algorithms into tracking pipelines. *Nat Methods* **19**, 829-832 (2022).
69. J. Y. Tinevez *et al.*, TrackMate: An open and extensible platform for single-particle tracking. *Methods* **115**, 80-90 (2017).
70. E. K. R. Mackay, S. Marbach, B. Sprinkle, A. L. Thorneywork, The Countoscope: Measuring Self and Collective Dynamics without Trajectories. *Phys Rev X* **14** (2024).
71. T. Ando, J. Skolnick, Crowding and hydrodynamic interactions likely dominate in vivo macromolecular motion. *Proc Natl Acad Sci U S A* **107**, 18457-18462 (2010).
72. A. P. Thompson *et al.*, LAMMPS-a flexible simulation tool for particle-based materials modeling at the atomic, meso, and continuum scales. *Comput Phys Commun* **271** (2022).
73. D. Reith, M. Pütz, F. Müller-Plathe, Deriving effective mesoscale potentials from atomistic simulations. *J Comput Chem* **24**, 1624-1636 (2003).

74. S. Kapishnikov *et al.*, Oriented nucleation of hemozoin at the digestive vacuole membrane in Plasmodium falciparum. *Proc. Natl. Acad. Sci. U. S. A.* **109**, 11188-11193 (2012).

Figure Legends

Figure 1: Quantification of hemozoin motion and its dependence on the FV environment. a, Diagram of a parasite-infected RBC, trafficking of host hemoglobin to the food vacuole, and formation of moving hemozoin crystals. **b**, Parasite FV regions of interest (inset) were imaged for variable exposure times. The pixel intensity change (Δ) in the region of interest was plotted versus time differences between frames. Heat map images (inset) show the gradient of pixel intensity changes, with yellow pixels indicating largest change and dark blue pixels indicating smallest change. Pixel intensity change dependence on frame rate was empirically fit to an exponential decay equation (black dotted line). Red dashed line indicates lower limit of background camera detection. **c**, Plots of time-averaged mean squared pixel intensity change (TAMSI) within the FV region as a function of elapsed time revealed a plateau (decorrelation) beyond 0.2 s. Data were fit with a power-law growth function, provided in Methods, to determine the average time to plateau. An apparent pixel velocity was determined by dividing the TAMSI value at the average plateau time of 0.18 s in native parasites (teal circle). **d**, Population analysis of pixel velocities for FVs in live, fractionated, or dead (drug-treated) parasites. Teal circle shows pixel velocity of FV analyzed in Fig. 1c. Dead parasites were treated with a lethal dose of chloroquine (shown) or other antimalarial drugs. Hemozoin motion stopped in all treatments. Statistical analysis was done by Student's t-test to determine the indicated p-values. Error bars represent the standard deviation of the mean.

Figure 2: Expanded food vacuoles enable single-particle tracking and reveal enhanced but confined motion. a, Hypotonic conditions increase FV radius by ≥2-fold while maintaining crystal motion but avoiding crystal overlap (**Movie S4**). FV crystals are compared to isolated crystals in media with defined viscosities. Individual particle tracking showing longest tracks. Scale bars = 2 μm. **b**, Time-averaged mean squared displacement (TAMSD) of hemozoin crystals in expanded FVs compared to free hemozoin in matched viscosity and water with fit values from Table S1. Error bars represent the standard deviation of the means of individual trajectories and are shown in grey. **c**, Diffusion profile scheme showing generalized interpretations of TAMSD analysis. Γ is generalized diffusion coefficient ($\mu m^2/s^\alpha$), α is power law exponent. **d**, Histogram showing probability density of average step size (distance traveled) of each crystal over normalized time. Steps were normalized by dividing by square root time between beginning and end of step (due to varying elapsed times in data set). Maroon bins show overlapping data in probability distributions.

Figure 3: Stochastic Brownian dynamics simulations of hemozoin crystal motion in distinct environments cannot account for anomalous FV features. a, Different geometric shapes and particle-particle interactions were used to compare Brownian models. Model 1 used cuboidal bricks with a repulsive Lennard-Jones interaction within a contact distance of 500 nm. Cuboidal

shapes used dimensions as shown following previous literature (4, 74). Model 2 used simplified spheres of equal crystal volume with a full Lennard-Jones potential including attraction and repulsion. **b**, Experimental tracks were used to calculate the interaction potentials between crystals. The calculated interaction potential looked like a fully defined Lennard-Jones potential with weak attraction and then repulsion at the minimal distance between two crystals. Model 2 used these interaction potentials. Inset shows probability of crystal-crystal distance in experiment vs. in an ideal gas scenario. **c**, TAMSD of hemozoin crystals in expanded FVs compared to simulations from Models 1 and 2 from Fig. 3A. See Tables S6 - S8 for fitted TAMSD values. Error bars represent the standard deviation of the means of individual trajectories and are shown in grey.

Figure 4: Extra energy and smaller confinement are required to capture crystal trajectories in the FV. a, Diagram showing predicted TAMSD plots for variable confinement radii. **b**, TAMSD of hemozoin crystals and inert nanobeads in water versus 15% aqueous H_2O_2. Error bars represent the standard deviation of the means of individual trajectories and are shown in grey. See Table S1 for fitted TAMSD values. **c**, Histograms showing probability density of average step size of each crystal over normalized time. Maroon bins show overlapping data in probability distributions. Solid curve is the step-size distribution predicted by our model of propulsive activity due to H_2O_2 catalysis. **d**, TAMSD of hemozoin crystals in expanded FVs compared to particles simulated with Brownian motion trajectories, experimental interaction potentials, confinement derivation from diagram in Fig. 4A and distribution of step sizes from Fig. 4C. See Table S8 for fitted TAMSD values. Error bars represent the standard deviation of the means of individual trajectories and are shown in grey. **e**, Population analysis of time-averaged mean squared pixel intensity change (TAMSI) of a FV in the specified conditions. Statistical analysis was done by Student's t-test to determine p-values. **f**, Scheme depicting both stimulation and micro-confinement to explain hemozoin crystal trajectories in the FV. Inset: Pink compartments depict possible vesicle remnants within the FV matrix that confine hemozoin motion.

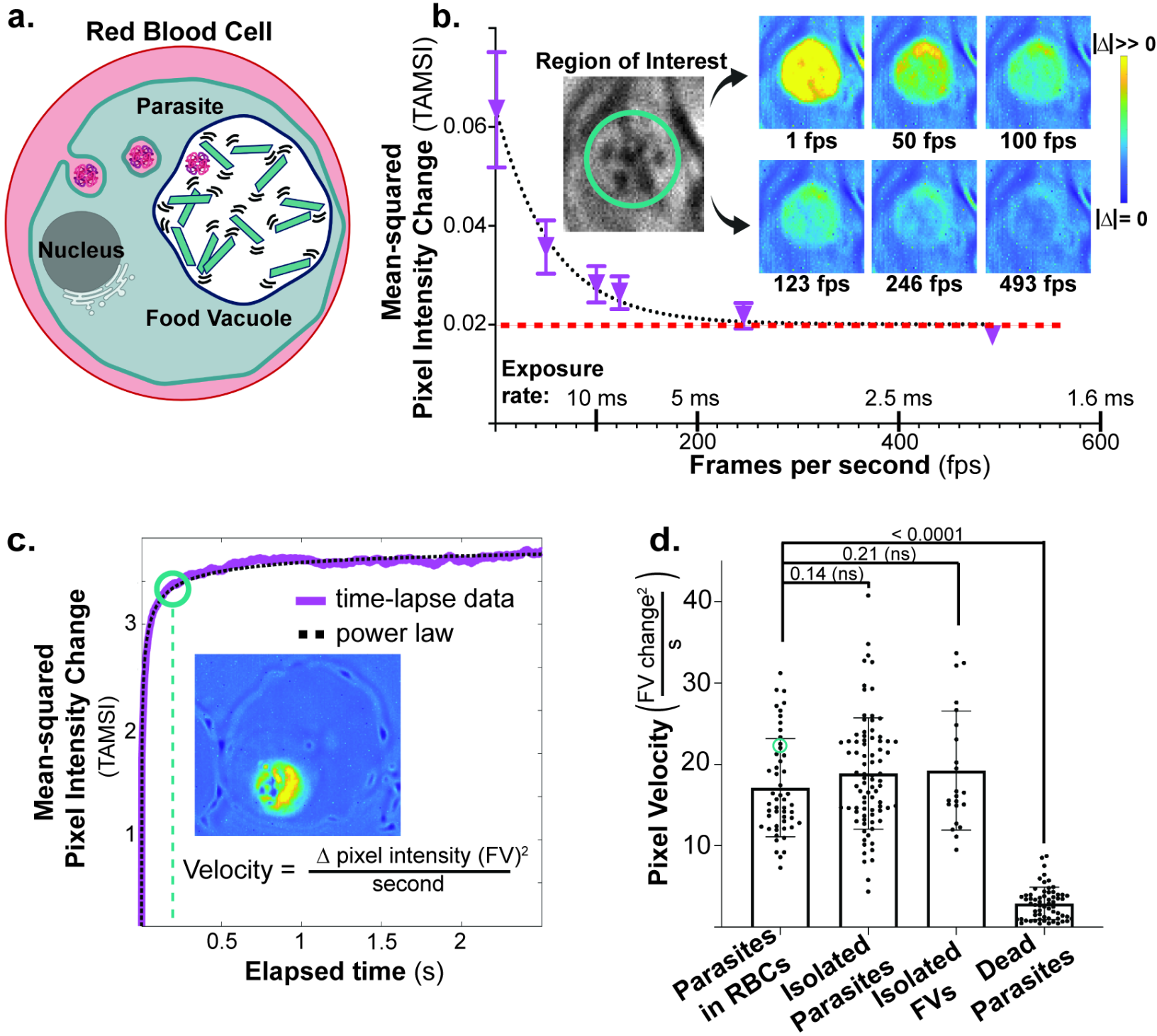
a.
Red Blood Cell
Parasite
Nucleus
Food Vacuole
b.
Region of Interest
Mean-squared Pixel Intensity Change (TAMSI)
0.06
0.04
0.02
1 fps
50 fps
100 fps
123 fps
246 fps
493 fps
|Δ|>> 0
|Δ|= 0
Exposure rate:
10 ms
5 ms
2.5 ms
1.6 ms
200
400
600
Frames per second (fps)
c.
Mean-squared Pixel Intensity Change (TAMSI)
time-lapse data
power law
Velocity = Δ pixel intensity (FV)² / second
0.5
1
1.5
2
Elapsed time (s)
d.
< 0.0001
0.21 (ns)
0.14 (ns)
Pixel Velocity (FV change² / s)
40
30
20
10
Parasites in RBCs
Isolated Parasites
Isolated FVs
Dead Parasites

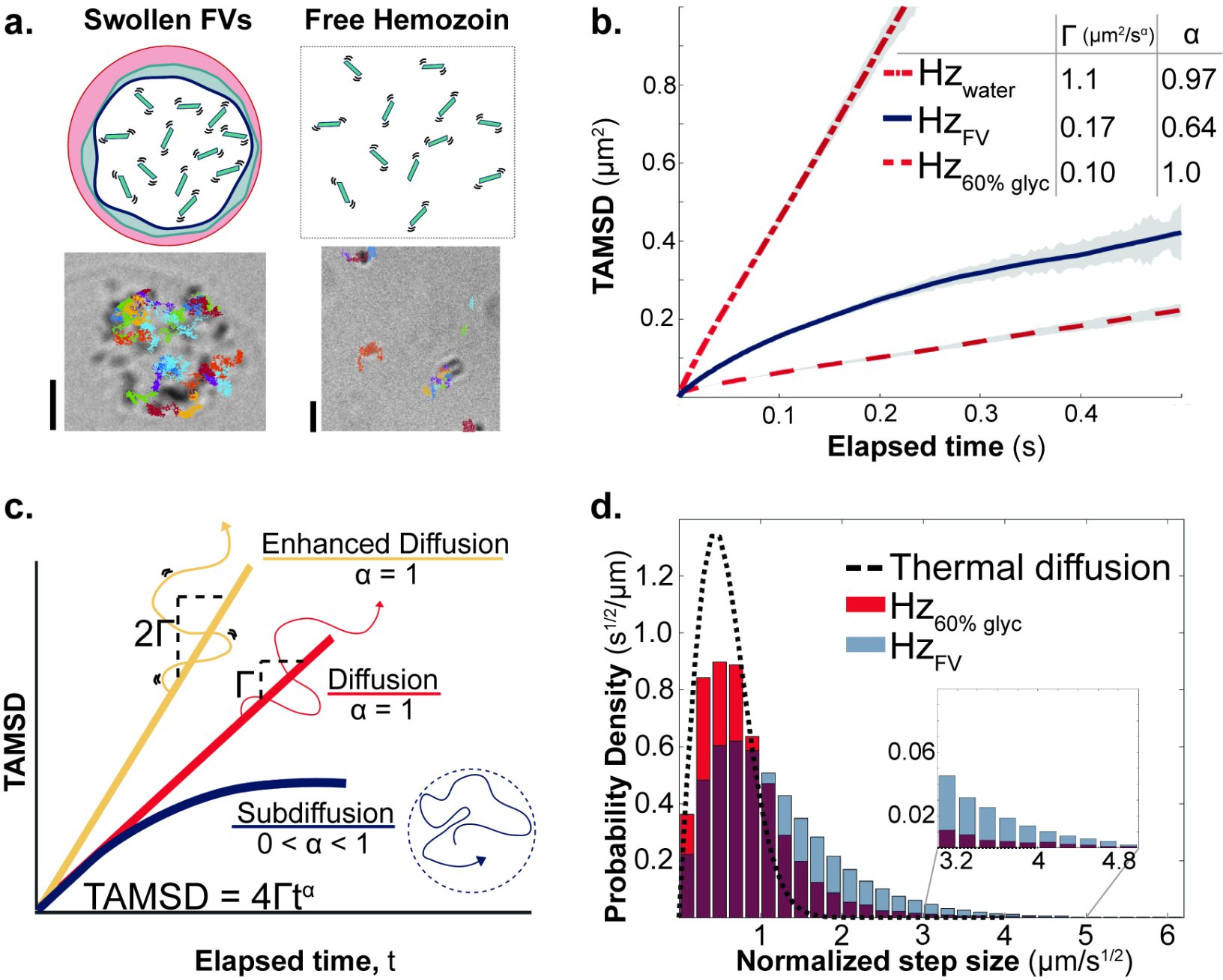
a.
Swollen FVs
Free Hemozoin
b.
TAMSD (μm²)
Elapsed time (s)
Γ (μm²/sᵃ)
α
Hz water 1.1 0.97
Hz FV 0.17 0.64
Hz 60% glyc 0.10 1.0
c.
Enhanced Diffusion
α = 1
2Γ
Γ
Diffusion
α = 1
Subdiffusion
0 < α < 1
TAMSD = 4Γtᵃ
TAMSD
Elapsed time, t
d.
Thermal diffusion
Hz 60% glyc
Hz FV
Probability Density (s^1/2/μm)
Normalized step size (μm/s^1/2)

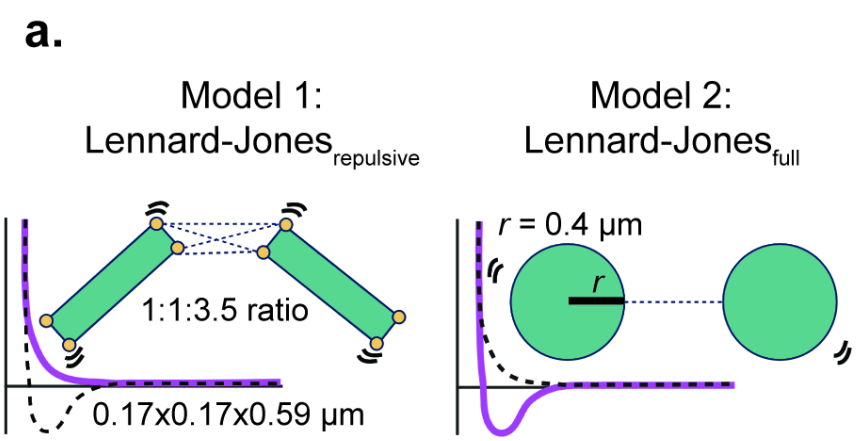

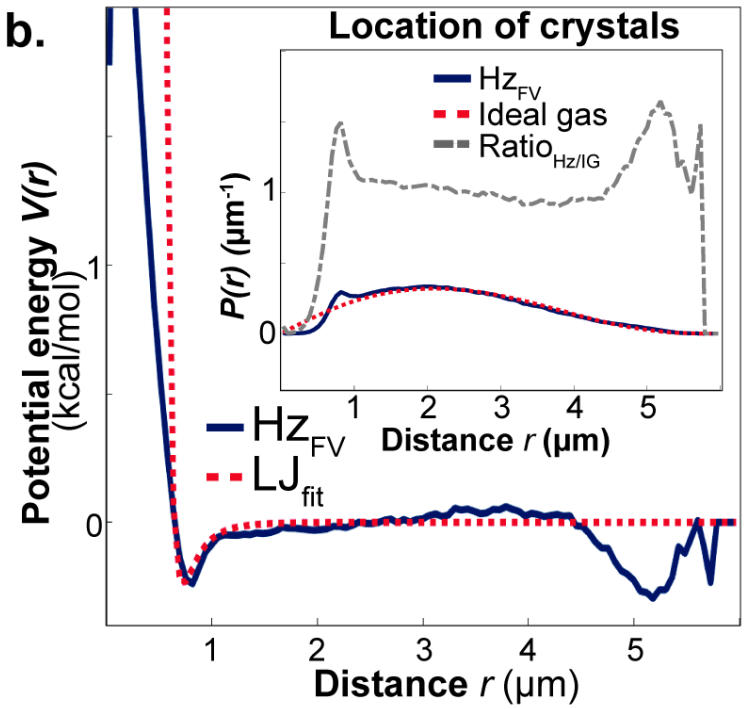

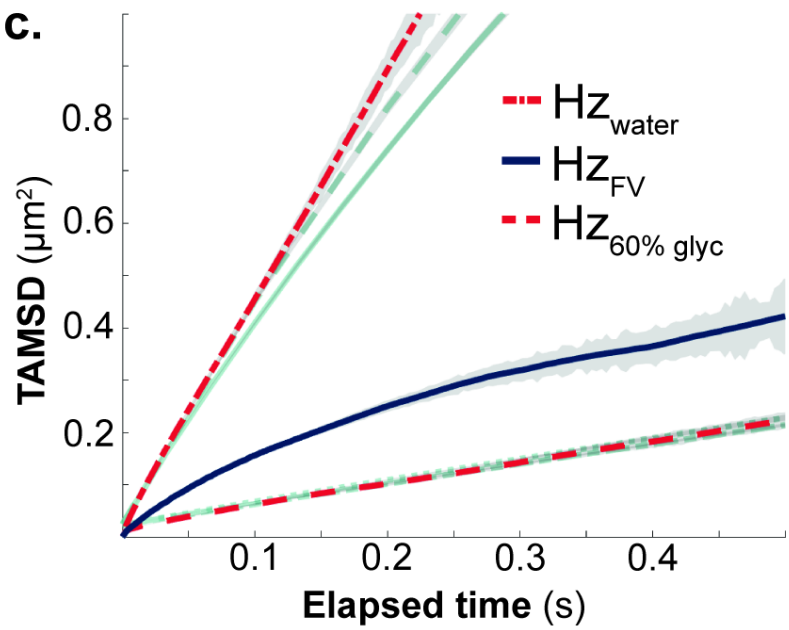

	Γ (µm²/sᵃ)	α
$Sim^{Model\ 2}_{water}$	0.83	0.89
$Sim^{Model\ 1}_{water}$	0.70	0.85
$Sim^{Model\ 2}_{60\%\ glyc}$	0.10	0.95
$Sim^{Model\ 1}_{60\%\ glyc}$	0.095	0.98

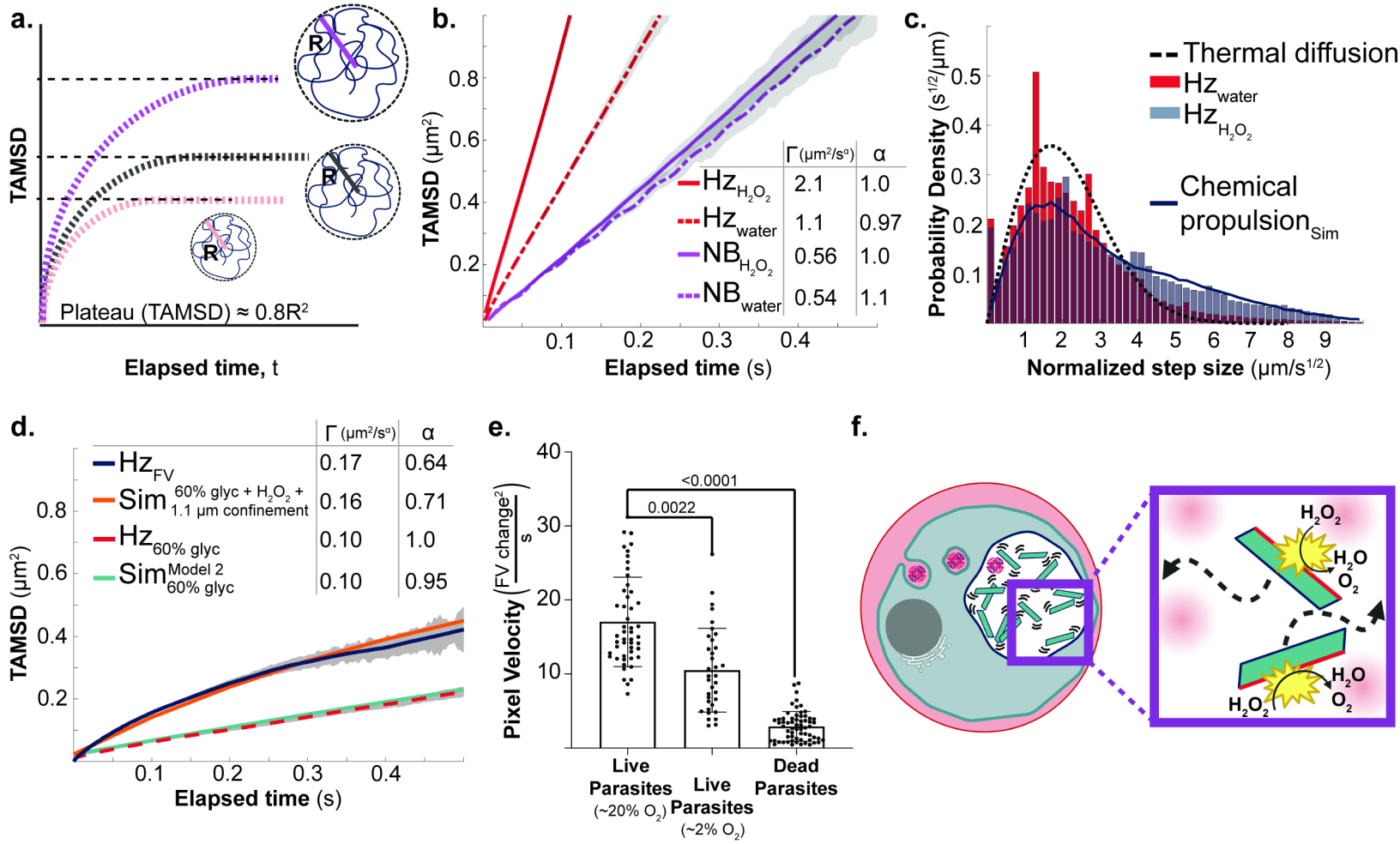
a.
TAMSD
R
R
R
Plateau (TAMSD) ≈ 0.8R²
Elapsed time, t
b.
TAMSD (μm²)
0.8
0.6
0.4
0.2
0.1
0.2
0.3
0.4
Elapsed time (s)
Γ (μm²/sᵃ) α
Hz H2O2 2.1 1.0
Hz water 1.1 0.97
NB H2O2 0.56 1.0
NB water 0.54 1.1
c.
Probability Density (s^1/2/μm)
0.5
0.4
0.3
0.2
0.1
1 2 3 4 5 6 7 8 9
Normalized step size (μm/s^1/2)
Thermal diffusion
Hz water
Hz H2O2
Chemical propulsion Sim
d.
Γ (μm²/sᵃ) α
Hz FV 0.17 0.64
Sim 60% glyc + H2O2 + 1.1 μm confinement 0.16 0.71
Hz 60% glyc 0.10 1.0
Sim Model 2 60% glyc 0.10 0.95
TAMSD (μm²)
0.8
0.6
0.4
0.2
0.1
0.2
0.3
0.4
Elapsed time (s)
e.
Pixel Velocity (FV change²/s)
40
30
20
10
<0.0001
0.0022
Live Parasites (~20% O2)
Live Parasites (~2% O2)
Dead Parasites
f.
H2O2
H2O
O2
H2O2
H2O
O2